

Learning Frequency-aware Dynamic Network for Efficient Super-Resolution

Wenbin Xie^{1,2*}, Dehua Song^{1*}, Chang Xu³, Chunjing Xu¹, Hui Zhang², Yunhe Wang¹

¹ Noah's Ark Lab, Huawei Technologies. ² School of Software, Tsinghua University. ³ The University of Sydney.

{dehua.song, yunhe.wang, xuchunjing}@huawei.com; xiewb18@mail.tsinghua.edu.cn;

Abstract

Deep learning based methods, especially convolutional neural networks (CNNs) have been successfully applied in the field of single image super-resolution (SISR). To obtain better fidelity and visual quality, most of existing networks are of heavy design with massive computation. However, the computation resources of modern mobile devices are limited, which cannot easily support the expensive cost. To this end, this paper explores a novel frequency-aware dynamic network for dividing the input into multiple parts according to its coefficients in the discrete cosine transform (DCT) domain. In practice, the high-frequency part will be processed using expensive operations and the lower-frequency part is assigned with cheap operations to relieve the computation burden. Since pixels or image patches belong to low-frequency areas contain relatively few textural details, this dynamic network will not affect the quality of resulting super-resolution images. In addition, we embed predictors into the proposed dynamic network to end-to-end fine-tune the handcrafted frequency-aware masks. Extensive experiments conducted on benchmark SISR models and datasets show that the frequency-aware dynamic network can be employed for various SISR neural architectures to obtain the better tradeoff between visual quality and computational complexity. For instance, we can reduce the FLOPs of SR models by approximate 50% while preserving state-of-the-art SISR performance.

1. Introduction

Single image super resolution (SISR) receives low-resolution images and outputs their high-resolution counterparts, which is widely used in real-world applications such as mobile phone, surveillance, autonomous driving, *etc.* Basically, SISR is an ill-posed reverse problem for recovering more information from the low-resolution versions. Thanks to the great progress of deep learning, a number of approaches have been explored using deep convolutional

*Equal contribution

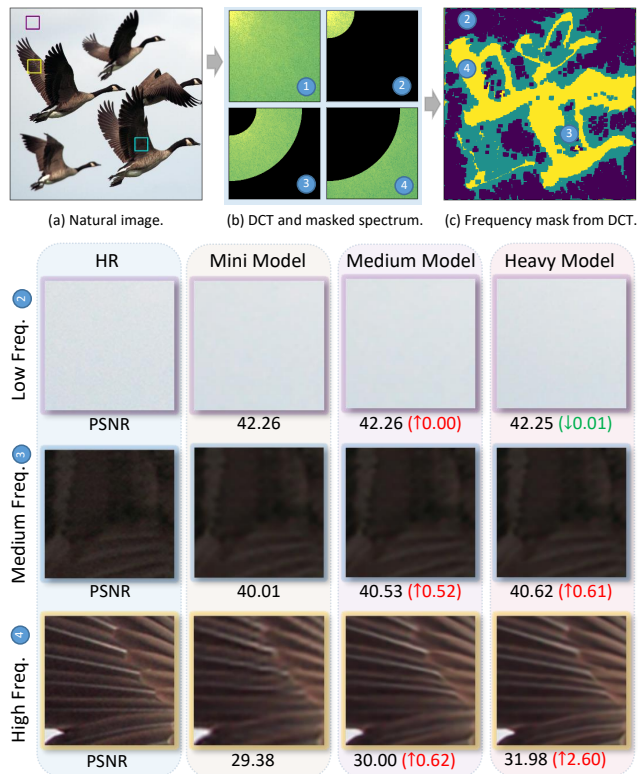


Figure 1: The motivation of our frequency-aware dynamic network. We illustrate the performance of SISR networks with various amounts of computation separately processing patches with different frequency signals. The profit brought by heavy computations becomes slighter as the frequency decreases. For conventional SR models, massive computation redundancy exists in processing low and medium frequency regions. Wherein, ②, ③ and ④ denote low, medium and high frequency signals/regions, respectively.

neural networks (CNNs) for addressing the SISR problem. Since neural networks can capture more information from a large amount of available images thus yield higher performance over conventional image recovery algorithms.

Similar to most computer vision tasks, the design of network architectures is quite important for the performance of SISR. Dong *et al.* [8] first employed a network on super-

resolution with only three convolutional layers, which obtained better performance than traditional methods. Subsequently, a series of networks with sophisticated architectures and loss functions are developed. For instance, Lim *et al.* [21] deepened the SR network with 32 res-blocks. Tai *et al.* [29] and Zhang *et al.* [38] investigated the dense concatenation on SR. In addition, channel attention (*e.g.*, RCAN [37] and SAN [7]) and spatial attention (*e.g.*, ABPN [23]) mechanisms were also embedded in SISR models and boosted the performance significantly.

Although tremendous efforts have been made to refine quantitative results *i.e.*, PSNR (Peak Signal-to-Noise Ratio) and SSIM (Structure Similarity), and visual quality of generated high-resolution images, the computational cost should be carefully restrained for real-world applications. For instance, 10,194G FLOPs is required for generating a 1280×720 (720p) image using RDN [27] model. To improve the model efficiency for deploying them on mobile devices while retaining the performance, Ahn *et al.* [2] and Luo *et al.* [24] employed cheap operators to construct efficient SR models manually. Furthermore, Chu *et al.* [6] and Song *et al.* [27] explored neural architecture search (NAS) to acquire efficient SISR networks automatically.

Nevertheless, most of existing approaches focus on reducing computation by processing the whole image with the same way, which are not perfectly efficient. Natural images are composed of distinct frequency signals according to the Fourier Transform [4]. Recovering high frequency information requires massive computations due to its severe damage during the downsample procedure, but reconstructing low frequency information does not demand such huge computations. Fig. 1 illustrates this phenomenon and indicates that the profit brought by heavy computations becomes slighter as the frequency decreases. Hence, massive computation redundancy exists in processing low and medium frequency regions. It motivates us to explore a more efficient SR method according to frequencies of the input instance.

To this end, this paper proposes a novel frequency-aware dynamic convolutional network (FADN). In each block, we introduce a predictor for dividing the input feature into multiple components based on the discrete cosine transform (DCT [1]) domain, *e.g.*, high-frequency, medium-frequency and low-frequency parts. The predictor is learned under the supervision of hand-crafted frequency-domain masks of images in the training set and the reconstruction loss of SISR, simultaneously. Then, features in these multiple parts will be processed using different convolutional layers with various computation burdens. The features with only low-frequency domain information will be assigned with cheaper operations for reducing computations and vice versa. Since features are divided into multiple branches in our paradigm, the overall computational complexity will be significantly reduced by the optimized allocation.

Extensive experiments are carefully conducted to verify the effectiveness of the proposed frequency-aware dynamic network on mainstream super-resolution benchmarks. The experimental results demonstrate that our method is able to employ on different neural architectures for achieving comparable and even better super-resolution performance using fewer computations.

The rest of this paper is structured as follows: we firstly summarize the related works on super-resolution methods in Section 2. In Section 3, the proposed method is introduced in detail. Then, comparison experiments and ablation study are depicted in Section 4. At last, we draw conclusions of the paper in Section 5.

2. Related Work

SISR problem has been investigated broadly in the last decades and remarkable improvement has been acquired. We summarize and analyze various SR methods.

2.1. Superior Super-resolution Methods

Enormous super-resolution methods can be roughly divided into three categories: interpolation-based, reconstruction-based and learning-based methods. Interpolation methods are efficient but suffer from severe flaws of fidelity [16]. In order to generate flexible and sharp details, reconstruction-based methods exploit sophisticated prior knowledge to reconstruct the high-resolution image [34]. However, these methods are time-consuming and sensitive to the handcrafted parameters. Recently, deep learning methods have dramatically boosted the performance of SISR. Dong *et al.* [8] firstly introduced DCNNs to SISR with only three convolution layers, yet its performance was greatly superior to that of traditional methods. Then, many approaches exploited the depth of DCNNs to improve the fidelity of SISR further, such as VDSR [17], SRResNet [20], and EDSR [21]. In addition, MemNet [29] and RDN [38] also explored dense concatenation to fusion features with different receptive fields. Channel attention (*e.g.* RCAN [37], SAN [7]) and spatial attention (*e.g.* ABPN [23]) were both applied on super-resolution network for better recovery of details. Lately, non-local-based graph networks (*e.g.* GCDN [31], IGNN [39]) are becoming a new trend to recover the detailed textures. On the other hand, perceptual loss [15] and adversarial training strategy [20] were adopted to improve the visual quality.

2.2. Efficient Super-resolution Models

The fidelity of SISR has been promoted significantly while the computational cost increases rapidly too. Massive computations of networks severely limited its application on real-world mobile devices. Hence, many researchers shifted their attention to developing efficient SISR networks. Dong *et al.* [9] firstly accelerated SISR models by

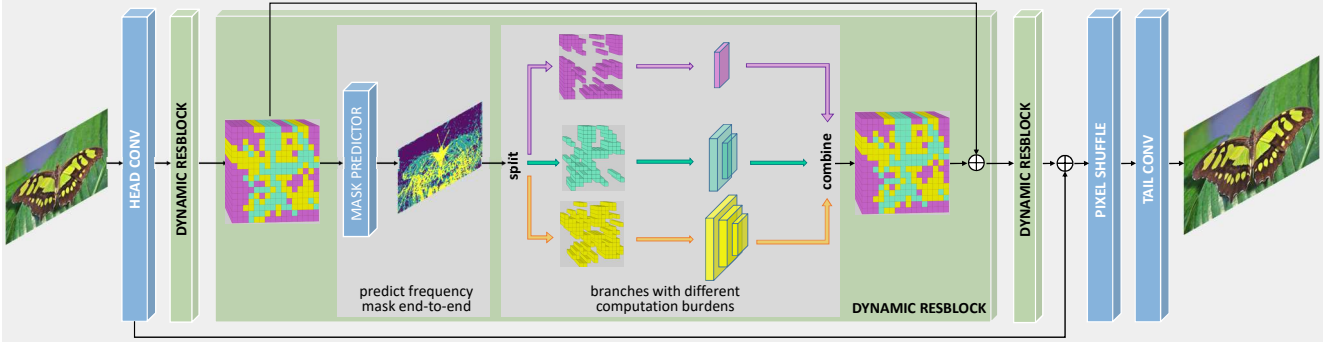


Figure 2: The overall framework of the proposed frequency-aware dynamic SR network (FADN).

delaying the upsample operation. Then, researchers began to design efficient blocks or networks with cheap operators, for example, CARN [2], IDN [13, 12] and LatticeNet [24]. To exploit efficient architecture thoroughly, neural architecture search (NAS) methods (*e.g.* FALSr [6], ESRN [27]) were employed to seek for extreme lightweight SISR networks. Besides, knowledge distillation technique [10, 35] was introduced to SISR to take full advantage of teacher network. Lately, quantization SISR networks [25, 33] were also explored with the assistance of feature complementary.

Besides, Liu *et al.* [22] designed a dynamic inference network to reduce computations, by predicting a depth mask and ignoring the calculations of partial features once the layer is deeper than the predicted depth. Note that the depth predictor cannot be optimized end-to-end. Verelst *et al.* [32] proposed a similar dynamic network that elides partial calculations for the classification task. These dynamic convolutions are totally designed on the spatial domain. Instead, we propose a novel dynamic mechanism based on the frequency-domain information in this paper. Our method recovers distinct frequency signals with branches requiring different computations and thus reduces the computational complexity.

3. Frequency-aware Dynamic Network

The framework of our proposed frequency-aware dynamic network is shown in Fig. 2. FADN consists of feature extraction, frequency-aware dynamic blocks (FADB) and reconstruction. Each dynamic block contains multiple branches with different computation burdens. In the inference stage, FADB automatically assigns higher frequency regions to heavier branches and lower frequency regions to lighter branches according to the learnable frequency mask.

3.1. Frequency-aware Dynamic Block

Firstly, we revisit prominent blocks in SR task, for example, resblock in EDSR [21] and channel attention resblock in RCAN [37]. The detail architectures of blocks are shown in Fig. 3. Block contains two 3×3 convolution and one

ReLU layers. In addition, RCAB also include a channel attention operator. Notating the input tensor as X and the output tensor as Y , RCAB can be modeled as

$$Y = X + CA(F), \quad (1)$$

where CA denotes the channel attention operator, F is output feature of the first two convolution layers, $F = f(X)$.

Channel attention averages the features across spatial space, hence our frequency-aware dynamic mechanism focuses on the feature transformation stage f . In the standard SR block, all pixels share same filters (*i.e.* filter size, number and weights). However, the pixels should not be treated equally in SR task, since high frequency signals suffer more seriously damage than low frequency signals during downscaling. In other words, low frequency signals can be recovered using cheap operations. Based on the idea, we design the frequency-aware dynamic block (FADB) which contains multiple branches with different burdens. In the inference stage, each pixel is assigned to a specific branch according to a learnable frequency-aware mask M . The number and detail structures of branches are optional. A typical FADB setting is shown in Fig. 3c which includes three branches. The heaviest branch is the same with standard block. The computations decrease gradually from left two branches to the right one. Notating the branch number as K and the function of branch k as f_k , the FADB can be represented as

$$F_i = \sum_{k=1}^K M_{i,k} \cdot f_k(X_i), \quad (2)$$

$$s.t. \ M_{i,k} \in \{0, 1\} \text{ and } \sum_k M_{i,k} = 1.$$

where i is the pixel index. The constraints mean that only one branch k where $M_{i,k} = 1$ will be chosen for X_i .

3.2. Mask Predictor

It's important to assign X_i to a proper branch according to the frequency strength so that lower frequency signals

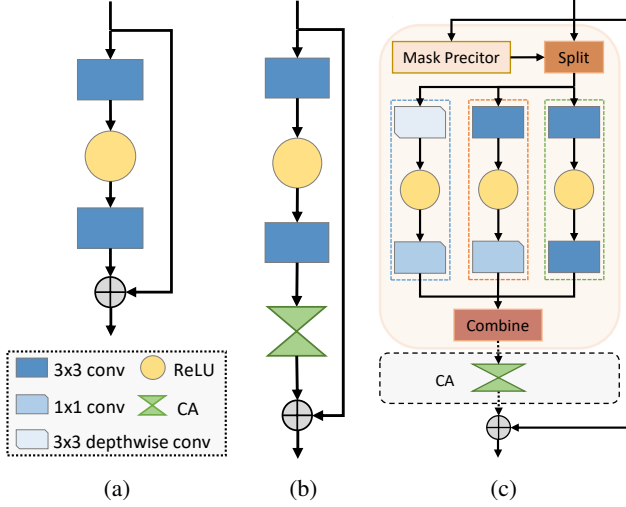


Figure 3: The structure of prominent SR blocks. (a) Block in EDSR [21]. (b) Block in RCAN [37] (CA operator stands for channel attention). (c) Corresponding frequency-aware dynamic block (CA is only employed in FAD-RCAN).

can be recovered using lighter branches to save computations. An intuitive strategy is to apply DCT type II [1, 28] to generate a frequency mask. We first use DCT to convert the image from spatial domain to frequency domain as shown in Fig. 1 (b-1) where the upper left parts are for low frequency signals and lower right parts are for high frequency signals. Then, we employ T frequency thresholds to separate the spectrum into $T + 1$ parts (e.g., 2 thresholds generate 3 spectrum parts as shown in Fig. 1 (b-2,3,4)). At last, these $T + 1$ spectrum parts are reconverted to spatial domain via IDCT, respectively, and generate the DCT frequency mask as shown in Fig. 1 (c). During the reconvolving stage, we process high frequency preferentially, i.e., once a pixel belongs to higher frequency, it won't be considered as lower frequency in the later processing. Hence, we usually generate DCT frequency mask from high frequency region to low frequency region sequentially.

Unfortunately, human-crafted thresholds are sensitive to noise and specific values are not suitable for all images. We expect the network can learn a frequency mask indicating which branch will be adopted by each pixel in an end-to-end manner. We make use of Gumbel Softmax trick [14] to make the mask prediction differentiable.

Given X , a 1×1 convolution is used as a simple mask predictor to generate a distribution D of K channels and same spatial size as X . The predictor is so small that its computational cost can be almost ignored. The frequency mask M can be calculated as

$$M_i = \text{one_hot}(\arg \max_k D_{i,k}). \quad (3)$$

Equation 3 has two drawbacks. First, it ignores the statis-

tic randomness as D is actually a continuous distribution instead of discrete variable. Second, it's not differentiable and hence can not be optimized end-to-end. Therefore, we apply Gumbel Softmax trick to get a continuous, differentiable normalized distribution:

$$G_i = \frac{\exp((D_i + g_i)/\tau)}{\sum_{k=1}^K \exp((D_{i,k} + g_{i,k})/\tau)}, \quad (4)$$

where g_i is drawn from $Gumbel(0, 1)$, τ is a temperature value controlling the distribution density and set as 1 in our experiments. The noise is only added in the training stage. We hope only one branch will be chosen for each pixel. In the forward process, the chosen branch (i.e. the frequency mask) is

$$M_i = \text{one_hot}(\arg \max_k G_{i,k}). \quad (5)$$

In order to train the predictor end-to-end, we calculate the gradient of M according to Equation 4 in the backward process, i.e.,

$$M_i = \begin{cases} \text{one_hot}(\arg \max_k G_{i,k}) & \text{forward,} \\ G_i & \text{backward.} \end{cases} \quad (6)$$

3.3. Loss

The proposed FADN is frequency-aware that models low frequency signals with cheaper operations. To this end, the mask predictor should absorb the prior knowledge from DCT frequency domain. Specifically, we make use of the frequency mask generated with DCT, notated as D , to guide the mask training. Assuming there are B dynamic res-blocks, the DCT loss is

$$L_{dct} = \sum_{b=1}^B CE(M_b, D), \quad (7)$$

where $CE(\cdot)$ is cross entropy loss and M_b is the predicted frequency mask of the b -th block.

Besides, it's important to control the computational cost conveniently for satisfying the requirements of various scenes. We realize that the sparsity of predicted frequency mask reflects the total computations, i.e., when the predicted frequency mask contains more low frequency components, the computational cost is smaller. Assuming there are n pixels in each block and c_k represents per-pixel FLOPs of branch k , the total FLOPs of a dynamic block are

$$C = \sum_{i=1}^n \sum_{k=1}^K M_{i,k} \cdot c_k. \quad (8)$$

The sparsity loss is designed as

$$L_{spa} = \left(\frac{\sum_{b=1}^B C_b}{B \cdot n c_K} - \alpha \right)^2, \quad (9)$$

where C_b is FLOPs of the b -th block, nc_K is FLOPs of a SR block and α is a hyper-parameter to control the frequency mask sparsity as well as the total FLOPs.

The total frequency mask loss is

$$L_{mask} = L_{spa} + \beta L_{dct}, \quad (10)$$

where β is a hyper-parameter to balance the two mask losses. We apply an annealing strategy on β and reduce it to zero gradually during training considering the following two reasons. First, the DCT frequency mask is not accurate since it is dependent on human-crafted thresholds and sensitive to noises. Second, L_{dct} cannot control the expected computations conveniently. Therefore, only L_{spa} is used to guide the mask learning in the later stage for better convergence and more precise control of computations.

To make the recovered images are of similar visual quality as the origin high resolution versions, we use L1 distance as the super-resolution loss:

$$L_{sr} = \|sr - hr\|_1, \quad (11)$$

where sr is the super-resolution image and hr is the ground truth as well as high-resolution image.

Finally, FADN is optimized by the two kinds of losses, L_{sr} for recovering more details and L_{spa} for guiding the predictor to learn the frequency distribution and control computational cost. The complete loss can be defined as

$$L = L_{mask} + L_{sr}. \quad (12)$$

3.4. Efficient Implementation

Since weight sharing is still kept along each branch, the calculation can be still implemented by GEMM [19] effectively. The first convolution in each branch should have same kernel size (*e.g.* 3) so that we can first apply *image2col* to unfold the input X . Meanwhile, the mask predictor generates frequency mask M . Then, the unfolded X is split and serves as the input of each branch according to M . The first convolution can be taken as the matrix multiplication between the unfolded input and kernel weight. 1×1 convolution and ReLU module is easy to implement since they are pixel-independent. The corresponding frequency mask should be dilated by a 3×3 kernel to keep receptive field if the branch includes two 3×3 convolution layers. After calculating the results of each branch, we combine them into an entire tensor.

3.5. Discussion

FADN vs. other spatially-varying computing methods Verelst *et al.* [32] proposed a dynamic mechanism by exploiting spatial sparsity for classification. It pays more computation on semantic contents and is not suitable for SISR task. AdaDSR [22] predicts the depth for each pixel directly. All these methods developed a sparse convolution

that neglects the calculations of partial input features once meeting certain conditions, which causes partial inputs cannot be modeled effectively. In contrast, based on the characteristics of SR illustrated in Fig. 1, our method takes full use of frequency-domain information to construct dynamic block since frequency has a positive relation with recovery difficulty of SR. Hence, the proposed FADN is quite different from other spatially-varying computing methods.

FADN vs. OctaveConv. The Octave convolution [5] separates the high-frequency and low-frequency with down-sample operations. In essence, the main idea of Octave convolution is consistent with multi-resolution feature representation. In contrast, the proposed dynamic network separates the regions with different frequency information according to mask predictor, which is consistent with DCT frequency information. Their main ideas are quite different.

4. Experiment

4.1. Implementation Details

Training We apply the proposed frequency-aware dynamic mechanisms on EDSR [21] and RCAN [37] models, which are called FAD-EDSR and FAD-RCAN, respectively. The DIV2K dataset [30] is adopted to train the dynamic networks. DIV2K includes 800 training images and 100 validation images. The low-resolution (LR) images are generated with bicubic degradation algorithm. The input patch size and data augmentation follow literature [21]. The training lasts 800,000 iterations and is optimized by ADAM algorithm [18] with $\beta_1 = 0.9$ and $\beta_2 = 0.999$. The initial learning rate is set to 0.01 for the mask predictor parameters, 0.0001 for other parameters (*i.e.* body parameters) and decays to half every 200,000 iterations. We set α as 0.4 and initialize β as 0.0001. We apply a linear annealing strategy on β which is reduced to 0 after 70% iterations.

Evaluation We evaluate our method with PSNR and SSIM metrics on four benchmarks: Set5 [3], Set14 [36], B100 [26] and Urban100 [11]. The PSNR and SSIM are calculated on the Y channel (*i.e.* the luminance channel) of YCbCr color space. The same amount of pixels as *scale* from the image boundary are ignored. The computational cost is evaluated by FLOPs (Floating Point of Operations).

4.2. Comparison with State-of-the-arts

To evaluate the effectiveness and efficiency of the proposed frequency-aware dynamic mechanism, we compare our experimental results with that of deep adaptive approach [22] (abbreviated as Ada-) on prominent EDSR [21] and RCAN [37] models. As shown in Table 1, compared with original SR model, our method reduces almost 50% of computations (*i.e.* FLOPs) while keeps and even increases the super-resolution accuracy (*i.e.* PSNR and SSIM). For instance, the FLOPs of EDSR on Set5 $\times 2$ are reduced by

Table 1: Quantitative results in comparison with the state-of-the-art methods on four benchmark databases. The best results are highlighted in bold.

| Scale | Method | Set5 | | | Set14 | | | B100 | | | Urban100 | | |
|-----------------|-----------------|----------------------|-----------------|------------------------|----------------------|-----------------|------------------------|----------------------|-----------------|------------------------|----------------------|-----------------|------------------------|
| | | PSNR \uparrow (dB) | SSIM \uparrow | FLOPs \downarrow (G) | PSNR \uparrow (dB) | SSIM \uparrow | FLOPs \downarrow (G) | PSNR \uparrow (dB) | SSIM \uparrow | FLOPs \downarrow (G) | PSNR \uparrow (dB) | SSIM \uparrow | FLOPs \downarrow (G) |
| $\times 2$ | Bicubic | 33.66 | 0.9299 | — | 30.24 | 0.8688 | — | 29.56 | 0.8431 | — | 26.88 | 0.8403 | — |
| | VDSR [17] | 37.53 | 0.9590 | 70.5 | 33.05 | 0.9130 | 143.0 | 31.90 | 0.8960 | 95.4 | 30.77 | 0.9140 | 481.6 |
| | EDSR [21] | 38.11 | 0.9601 | 1338.8 | 33.92 | 0.9195 | 2552.2 | 32.32 | 0.9013 | 1776.9 | 32.93 | 0.9351 | 8041.1 |
| | AdaEDSR [22] | 38.21 | 0.9611 | 650.6 | 33.97 | 0.9208 | 1397.3 | 32.35 | 0.9017 | 965.3 | 32.91 | 0.9353 | 4844.9 |
| | FAD-EDSR | 38.21 | 0.9611 | 408.4 | 33.95 | 0.9202 | 1068.8 | 32.33 | 0.9015 | 686.7 | 32.93 | 0.9353 | 4192.9 |
| | RCAN [37] | 38.27 | 0.9614 | 577.9 | 34.12 | 0.9216 | 1101.8 | 32.41 | 0.9027 | 767.0 | 33.34 | 0.9384 | 3471.2 |
| | AdaRCAN [22] | 38.28 | 0.9615 | 469.1 | 34.12 | 0.9216 | 751.9 | 32.41 | 0.9026 | 606.3 | 33.29 | 0.9380 | 2907.2 |
| FAD-RCAN | 38.29 | 0.9617 | 260.8 | 34.11 | 0.9215 | 512.6 | 32.42 | 0.9028 | 363.7 | 33.34 | 0.9385 | 2089.4 | |
| $\times 3$ | Bicubic | 30.39 | 0.8682 | — | 27.55 | 0.7742 | — | 27.21 | 0.7385 | — | 24.46 | 0.7349 | — |
| | VDSR [17] | 33.67 | 0.9210 | 70.5 | 29.78 | 0.8320 | 143.0 | 28.83 | 0.7990 | 95.4 | 27.14 | 0.8290 | 481.6 |
| | EDSR [21] | 34.65 | 0.9280 | 699.1 | 30.52 | 0.8462 | 1305.7 | 29.25 | 0.8093 | 924.1 | 28.80 | 0.8653 | 3984.0 |
| | AdaEDSR [22] | 34.65 | 0.9288 | 504.8 | 30.57 | 0.8463 | 1013.5 | 29.27 | 0.8091 | 722.8 | 28.78 | 0.8649 | 3314.2 |
| | FAD-EDSR | 34.69 | 0.9288 | 281.0 | 30.58 | 0.8467 | 651.5 | 29.27 | 0.8097 | 423.6 | 28.89 | 0.8668 | 2472.9 |
| | RCAN [37] | 34.74 | 0.9299 | 328.5 | 30.65 | 0.8482 | 613.5 | 29.32 | 0.8111 | 434.2 | 29.09 | 0.8702 | 1872.0 |
| | AdaRCAN [22] | 34.79 | 0.9302 | 277.7 | 30.65 | 0.8481 | 512.9 | 29.33 | 0.8111 | 369.3 | 29.03 | 0.8689 | 1596.3 |
| FAD-RCAN | 34.82 | 0.9304 | 141.2 | 30.66 | 0.8485 | 306.1 | 29.33 | 0.8112 | 212.3 | 29.12 | 0.8706 | 1081.6 | |
| $\times 4$ | Bicubic | 28.42 | 0.8104 | — | 26.00 | 0.7027 | — | 25.96 | 0.6675 | — | 23.14 | 0.6577 | — |
| | VDSR [17] | 31.35 | 0.8830 | 70.5 | 28.02 | 0.7680 | 143.0 | 27.29 | 0.0726 | 95.4 | 25.18 | 0.7540 | 481.6 |
| | EDSR [21] | 32.46 | 0.8968 | 501.9 | 28.80 | 0.7876 | 908.8 | 27.71 | 0.7420 | 655.7 | 26.64 | 0.8033 | 2699.4 |
| | AdaEDSR [22] | 32.49 | 0.8977 | 371.7 | 28.76 | 0.7865 | 716.8 | 27.71 | 0.7410 | 508.5 | 26.58 | 0.8011 | 2265.8 |
| | FAD-EDSR | 32.50 | 0.8977 | 218.1 | 28.82 | 0.7880 | 471.7 | 27.73 | 0.7438 | 304.6 | 26.70 | 0.8049 | 1729.9 |
| | RCAN [37] | 32.63 | 0.9002 | 270.1 | 28.87 | 0.7889 | 489.0 | 27.77 | 0.7436 | 352.8 | 26.82 | 0.8087 | 1452.5 |
| | AdaRCAN [22] | 32.61 | 0.8998 | 277.5 | 28.88 | 0.7883 | 418.1 | 27.77 | 0.7428 | 304.8 | 26.80 | 0.8067 | 1263.0 |
| FAD-RCAN | 32.65 | 0.9007 | 115.4 | 28.88 | 0.7889 | 258.3 | 27.78 | 0.7437 | 169.8 | 26.86 | 0.8092 | 891.2 | |

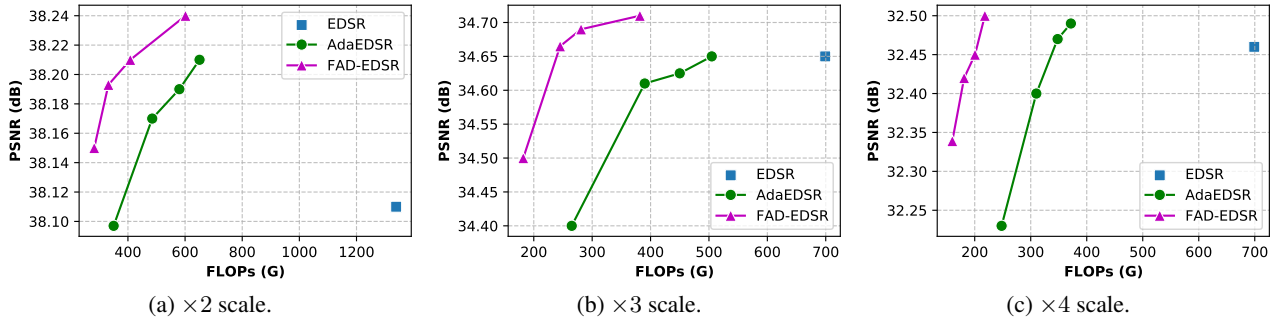


Figure 4: Comparison to state-of-the-art methods in terms of PSNR and FLOPs. The benchmark used is Set5.

69.6% while PSNR is improved by 0.11dB. Compared to deep adaptive approach (*i.e.* AdaEDSR and AdaRCAN), our method reduces more computation and gets better SR accuracy. Taking the experiment on B100 with $\times 4$ scale as example, the FLOPs of AdaEDSR are reduced by 22.4% and PSNR is similar to EDSR. In contrast, the FLOPs of our model are reduced more, *i.e.* 53.5%, while PSNR is increased by 0.02dB. An interesting phenomenon is that AdaEDSR meets a serious performance degradation in large-scale upscaling (*i.e.* $\times 3$ and $\times 4$) whose optimizations are harder than $\times 2$ upscaling since the larger-scale downscaling causes more high frequency signals lost. However, our methods still keeps excellent performance because of

the end-to-end optimization and coordinated branches. We also evaluated the latency of the proposed frequency-aware dynamic models on CPU platform with different number of cores. The experimental results in Table 2 show that the proposed method reduces the latency of model significantly.

In addition to the quantitative results, we visual the super-resolution resulting images in Fig. 5 including two common scenes, *i.e.*, blurring and artifacts caused by serious downscaling (the first and second row respectively). The proposed method achieves very close even better visual quality compared with original model. The performance of our method outperforms that of deep adaptive mechanism significantly. We use α to control the computational cost as

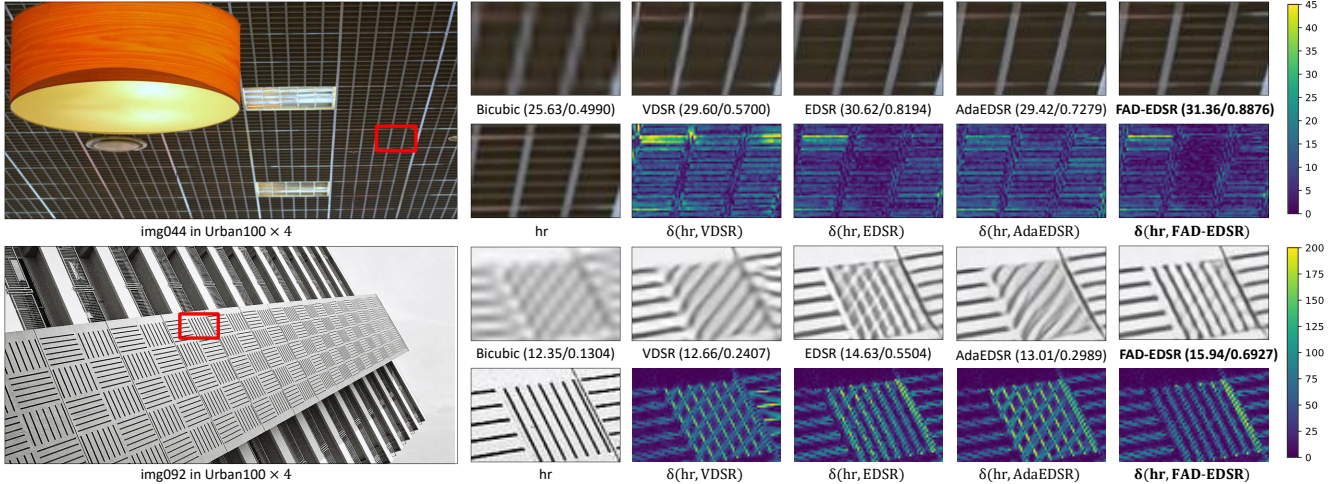


Figure 5: Visual Comparison with state-of-the-art methods. δ is the residual map of the two given images.

Table 2: Latency of various models executed on CPU.

| Platform | EDSR | FAD-EDSR | Speed-up ratio |
|-----------------|--------|----------|----------------|
| Single core CPU | 39.60s | 25.44s | $\times 1.6$ |
| Double core CPU | 20.08s | 13.74s | $\times 1.5$ |

Table 3: Comparison of various frequency masks on EDSR-baseline [21]. PSNR is reported and scale factor is $\times 2$.

| Methods | Set5 | Set14 | B100 | Urban100 |
|------------------------|--------------|--------------|--------------|--------------|
| Random for blocks | 37.79 | 33.33 | 32.06 | 31.47 |
| Random for images | 37.67 | 33.19 | 31.95 | 31.17 |
| DCT mask | 37.82 | 33.40 | 32.07 | 31.72 |
| Learnable w/o guidance | 37.86 | 33.43 | 32.11 | 31.81 |
| Learnable w/ guidance | 37.92 | 33.49 | 32.13 | 31.90 |

shown in Equation 9. Multiple models with different computations are obtained by adjusting the hyper-parameter and the relation between PSNR and FLOPs is shown in Fig. 4. The upper left points have better performance. One can see that the proposed method outperforms its counterparts.

Why did FADN achieve higher accuracy over baselines?

The proposed FADN possesses more parameters compared with the original baseline. In addition, the branching strategy allows the weights of each branch to adapt to the specific frequency region instead of covering various frequency regions. Finally, cheap operator can achieve better accuracy than heavy operator on low-frequency regions. Hence, our method achieves better performance than the SR baselines.

More prominent SISR models are evaluated in the [Supplementary Material](#). It shows that the proposed method reduces FLOPs significantly while preserves the performance.

4.3. Ablation Study

In ablation study, we apply our method on EDSR baseline [21] which includes 16 residual blocks of 64 channels.

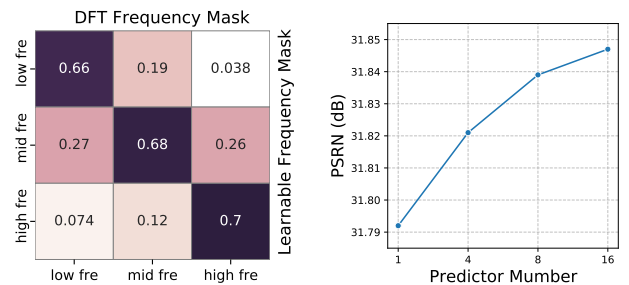


Figure 6: Confusion Matrix between DCT and learnable frequency mask. Figure 7: Comparison of different predictor number. PSNR in Urban $\times 2$ is reported.

All models are trained for 300,000 iterations and the learning rate decays to half every 100,000 iterations. Note that We have adjusted the hyper-parameter α and guaranteed the computations among each experiment are comparable.

Learnable Frequency Mask The frequency masks are learned by an end-to-end manner in our proposed methods. To demonstrate the effectiveness of learnable frequency masks, we exploit different strategies for mask generation, including *random masks for each block*, *random masks for each image* (i.e., *sharing a fixed random mask among blocks*), *fixed frequency masks generated by DCT*, *learnable frequency masks without DCT guidance* and *learnable frequency masks with DCT guidance*. Note that we are more concerned about the performance on Urban100 since its image quantity and quality are higher. As shown in Table. 3, the performance using random masks is terrible because the model cannot identify the frequency information and assign pixels to the reasonable branches. A fixed random mask is worse than multiple random masks among blocks. The DCT frequency masks outperform random masks because the former provide appropriate indication that assigns pixels to the proper branches. However, the DCT frequency masks are dependent on human-crafted thresholds and sen-

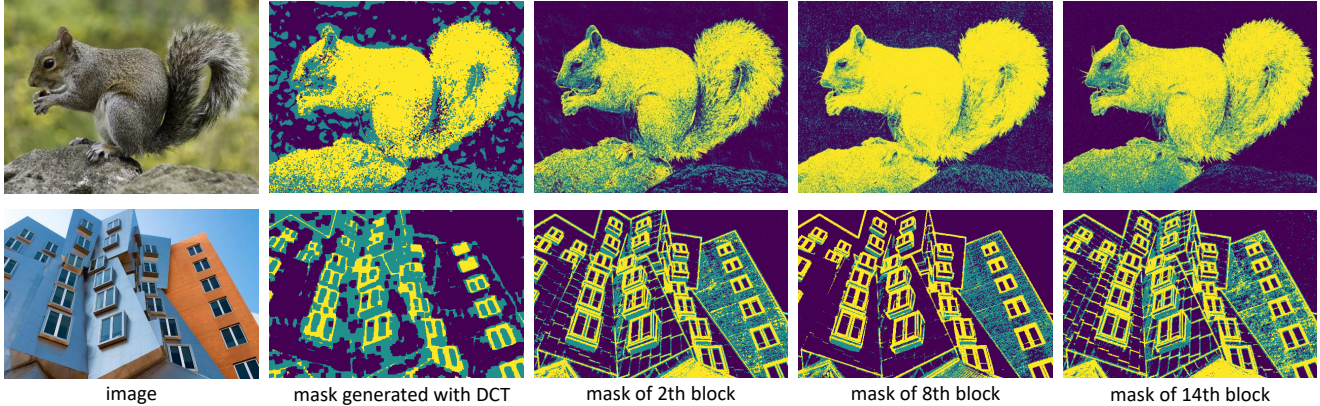


Figure 8: Comparison between frequency masks generated with DCT and our learnable frequency masks in different blocks. Yellow, Blue and Purple represent High, Medium and Low frequency respectively.

sitive to noise. Besides, the specific thresholds cannot adapt to all images. The learnable frequency masks avoid the problem by end-to-end optimization. Without the guidance of DCT prior knowledge, learnable frequency masks outperform DCT frequency masks. With the help of guidance, models can converge faster and achieve better performance.

Apart from the quantitative performance comparison, we compare the learnable frequency masks with DCT frequency masks. As shown in Fig. 8, DCT frequency masks indicate the frequency distribution but are sensitive to noises. Our learnable frequency masks are similar to the DCT frequency masks except for minority regions where the predictor adjusts the mask according to specific inputs for more accurate indication. Besides, the learnable frequency masks are little different among each block since it’s not a wise choice to use a fixed frequency mask for all blocks. Generally, the lower frequency pixels tend to use the branches requiring less computations. The result implies the proposed FADN model can identify the frequency strength and assign the pixels to branches of proper computations according to the frequency strength. The confusion matrix between DCT frequency masks and learnable frequency masks is shown in Fig. 6 which also proves that the mask predictor can learn the frequency distribution and adjust the partition thresholds automatically.

Mask Predictor Number By default, we use a separate mask predictor for each frequency-aware dynamic block. Besides, the predictor can also be shared among multiple blocks. We visualize the influence of predictor number in Figure 7. In particular, the model learns one frequency mask for the whole network when the predictor number is 1 and learns an independent mask for each block when the number is 16. One can see that a single predictor performs worse than multiple predictors, because the optimal frequency partition is not invariant among blocks. It is another important reason why we can not use the fixed frequency masks generated with DCT directly. Overall, as the

Table 4: Comparison of different branch number. PSNR is reported and scale factor is $\times 2$.

| Branch Num. | Set5 | Set14 | B100 | Urban100 |
|-------------|--------------|--------------|--------------|--------------|
| 2 | 37.84 | 33.44 | 32.09 | 31.72 |
| 3 | 37.90 | 33.47 | 32.13 | 31.85 |
| 4 | 37.90 | 33.48 | 32.12 | 31.88 |

predictor number increases, the adjustment ability of FADN is more powerful. The performance therefore becomes better although the improvement grows more slowly.

Branch Number We use 3-branch FADN in above experiments but the branch number and branch architectures are optional. We test the influence of different branch number. As the branch number increases, each branch only needs to recover signals in a smaller frequency range. The results are shown in Table. 4. Note that we have guaranteed similar computations among different settings. The performance of 3-branch is significantly better than 2-branch while 4-branch is slightly better than 3-branch. Considering the storage cost, 3-branch FADN are recommended.

5. Conclusion

In this paper, a novel frequency-aware dynamic network (FADN) is proposed for efficient single image super resolution, which assigns cheap operations to low-frequency regions and vice visa. To this end, a predictor is introduced to divide the input feature into multiple components based on DCT domain. The predictor is learned under the supervision of hand-crafted frequency-domain masks of images in the training set and the reconstruction loss of SISR, simultaneously. The overall computational complexity will be significantly reduced by the optimized allocation. In addition, the frequency-aware dynamic mechanism can be conveniently employed on various SISR architectures. Experimental results indicate that FADN can effectively reduce approximate half of FLOPs in multiple benchmark databases while maintaining the performance of the original network.

References

- [1] Nasir Ahmed, T Natarajan, and Kamisetty R Rao. Discrete cosine transform. *IEEE transactions on Computers*, 100(1):90–93, 1974. [2](#), [4](#)
- [2] Namhyuk Ahn, Byungkon Kang, and Kyung-Ah Sohn. Fast, accurate, and lightweight super-resolution with cascading residual network. In *ECCV*, pages 252–268, 2018. [2](#), [3](#)
- [3] Marco Bevilacqua, Aline Roumy, Christine Guillemot, and Marie Line Alberi-Morel. Low-complexity single-image super-resolution based on nonnegative neighbor embedding. 2012. [5](#)
- [4] Ronald Newbold Bracewell and Ronald N Bracewell. *The Fourier transform and its applications*, volume 31999. McGraw-Hill New York, 1986. [2](#)
- [5] Yunpeng Chen, Haoqi Fan, Bing Xu, Zhicheng Yan, Yan-nis Kalantidis, Marcus Rohrbach, Shuicheng Yan, and Jiashi Feng. Drop an octave: Reducing spatial redundancy in convolutional neural networks with octave convolution. In *Proceedings of the IEEE/CVF International Conference on Computer Vision*, pages 3435–3444, 2019. [5](#)
- [6] Xiangxiang Chu, Bo Zhang, Hailong Ma, Ruijun Xu, Jixiang Li, and Qingyuan Li. Fast, accurate and lightweight super-resolution with neural architecture search. *arXiv preprint arXiv:1901.07261*, 2019. [2](#), [3](#)
- [7] Tao Dai, Jianrui Cai, Yongbing Zhang, Shu-Tao Xia, and Lei Zhang. Second-order attention network for single image super-resolution. In *Proceedings of the IEEE conference on computer vision and pattern recognition*, pages 11065–11074, 2019. [2](#)
- [8] Chao Dong, Chen Change Loy, Kaiming He, and Xiaoou Tang. Learning a deep convolutional network for image super-resolution. In *ECCV*, pages 184–199, 2014. [1](#), [2](#)
- [9] Chao Dong, Chen Change Loy, and Xiaoou Tang. Accelerating the super-resolution convolutional neural network. In *ECCV*, pages 391–407. Springer, 2016. [2](#)
- [10] Qinqun Gao, Yan Zhao, Gen Li, and Tong Tong. Image super-resolution using knowledge distillation. In *Asian Conference on Computer Vision*, pages 527–541. Springer, 2018. [3](#)
- [11] Jia-Bin Huang, Abhishek Singh, and Narendra Ahuja. Single image super-resolution from transformed self-exemplars. In *Proceedings of the IEEE conference on computer vision and pattern recognition*, pages 5197–5206, 2015. [5](#)
- [12] Zheng Hui, Xinbo Gao, Yunchu Yang, and Xiumei Wang. Lightweight image super-resolution with information multi-distillation network. In *Proceedings of the 27th ACM International Conference on Multimedia*, pages 2024–2032, 2019. [3](#)
- [13] Zheng Hui, Xiumei Wang, and Xinbo Gao. Fast and accurate single image super-resolution via information distillation network. In *CVPR*, pages 723–731, 2018. [3](#)
- [14] Eric Jang, Shixiang Gu, and Ben Poole. Categorical reparameterization with gumbel-softmax. *arXiv preprint arXiv:1611.01144*, 2016. [4](#)
- [15] Justin Johnson, Alexandre Alahi, and Li Fei-Fei. Perceptual losses for real-time style transfer and super-resolution. In *ECCV*, pages 694–711. Springer, 2016. [2](#)
- [16] Robert Keys. Cubic convolution interpolation for digital image processing. *IEEE transactions on acoustics, speech, and signal processing*, 29(6):1153–1160, 1981. [2](#)
- [17] Jiwon Kim, Jung Kwon Lee, and Kyoung Mu Lee. Accurate image super-resolution using very deep convolutional networks. In *CVPR*, pages 1646–1654, 2016. [2](#), [6](#)
- [18] Diederik P Kingma and Jimmy Ba. Adam: A method for stochastic optimization. 2014. [5](#)
- [19] Chuck L Lawson, Richard J. Hanson, David R Kincaid, and Fred T. Krogh. Basic linear algebra subprograms for fortran usage. *ACM Transactions on Mathematical Software (TOMS)*, 5(3):308–323, 1979. [5](#)
- [20] Christian Ledig, Lucas Theis, Ferenc Huszár, Jose Caballero, Andrew Cunningham, Alejandro Acosta, Andrew Aitken, Alykhan Tejani, Johannes Totz, Zehan Wang, et al. Photo-realistic single image super-resolution using a generative adversarial network. In *CVPR*, pages 4681–4690, 2017. [2](#)
- [21] Bee Lim, Sanghyun Son, Heewon Kim, Seungjun Nah, and Kyoung Mu Lee. Enhanced deep residual networks for single image super-resolution. In *CVPR Workshops*, pages 136–144, 2017. [2](#), [3](#), [4](#), [5](#), [6](#), [7](#)
- [22] Ming Liu, Zhilu Zhang, Liya Hou, Wangmeng Zuo, and Lei Zhang. Deep adaptive inference networks for single image super-resolution. In *European Conference on Computer Vision Workshop*, 2020. [3](#), [5](#), [6](#)
- [23] Zhi-Song Liu, Li-Wen Wang, Chu-Tak Li, Wan-Chi Siu, and Yui-Lam Chan. Image super-resolution via attention based back projection networks. In *International Conference on Computer Vision Workshop*, pages 3517–3525, 2019. [2](#)
- [24] Xiaotong Luo, Yuan Xie, Yulun Zhang, Yanyun Qu, Cuihua Li, and Yun Fu. Latticenet: Towards lightweight image super-resolution with lattice block. In *Proceedings of the European Conference on Computer Vision*, 2020. [2](#), [3](#)
- [25] Yinglan Ma, Hongyu Xiong, Zhe Hu, and Lizhuang Ma. Efficient super resolution using binarized neural network. In *CVPR Workshops*, pages 0–0, 2019. [3](#)
- [26] David Martin, Charless Fowlkes, Doron Tal, and Jitendra Malik. A database of human segmented natural images and its application to evaluating segmentation algorithms and measuring ecological statistics. In *ICCV*, volume 2, pages 416–423. IEEE, 2001. [5](#)
- [27] Dehua Song, Chang Xu, Xu Jia, Chunjing Xu, and Yunhe Wang. Efficient residual dense block search for image super-resolution. 2020. [2](#), [3](#)
- [28] Gilbert Strang. The discrete cosine transform. *SIAM review*, 41(1):135–147, 1999. [4](#)
- [29] Ying Tai, Jian Yang, Xiaoming Liu, and Chunyan Xu. Memnet: A persistent memory network for image restoration. In *ICCV*, pages 4539–4547, 2017. [2](#)
- [30] Radu Timofte, Eirikur Agustsson, Luc Van Gool, Ming-Hsuan Yang, and Lei Zhang. Ntire 2017 challenge on single image super-resolution: Methods and results. In *CVPR Workshops*, pages 114–125, 2017. [5](#)
- [31] Diego Valsesia, Giulia Fracastoro, and Enrico Magli. Deep graph-convolutional image denoising. *IEEE Transactions on Image Processing*, 29:8226–8237, 2020. [2](#)

- [32] Thomas Verelst and Tinne Tuytelaars. Dynamic convolutions: Exploiting spatial sparsity for faster inference. In *Proceedings of the IEEE/CVF Conference on Computer Vision and Pattern Recognition*, pages 2320–2329, 2020. 3, 5
- [33] Jingwei Xin, Nannan Wang, Xinrui Jiang, Jie Li, Heng Huang, and Xinbo Gao. Binarized neural network for single image super resolution. In *European Conference on Computer Vision*, 2020. 3
- [34] Qing Yan, Yi Xu, Xiaokang Yang, and Truong Q Nguyen. Single image superresolution based on gradient profile sharpness. *IEEE Transactions on Image Processing*, 24(10):3187–3202, 2015. 2
- [35] Yiding Yang, Jiayan Qiu, Mingli Song, Dacheng Tao, and Xinchao Wang. Distilling knowledge from graph convolutional networks. In *Proceedings of the IEEE/CVF Conference on Computer Vision and Pattern Recognition*, pages 7074–7083, 2020. 3
- [36] Roman Zeyde, Michael Elad, and Matan Protter. On single image scale-up using sparse-representations. In *International conference on curves and surfaces*, pages 711–730. Springer, 2010. 5
- [37] Yulun Zhang, Kungpeng Li, Kai Li, Lichen Wang, Bineng Zhong, and Yun Fu. Image super-resolution using very deep residual channel attention networks. In *Proceedings of the European Conference on Computer Vision*, pages 286–301, 2018. 2, 3, 4, 5, 6
- [38] Yulun Zhang, Yapeng Tian, Yu Kong, Bineng Zhong, and Yun Fu. Residual dense network for image super-resolution. In *CVPR*, pages 2472–2481, 2018. 2
- [39] Shangchen Zhou, Jiawei Zhang, Wangmeng Zuo, and Chen Change Loy. Cross-scale internal graph neural network for image super-resolution. In *Advances in neural information processing systems*, 2020. 2